Chinese Chemical Letters 34 (2023) 108140

Contents lists available at ScienceDirect

Chinese Chemical Letters

journal homepage: www.elsevier.com/locate/cclet

Size engineering of 2D MOF nanosheets for enhanced photodynamic antimicrobial therapy

Baoli Xue[a,b,c,1], Xiwen Geng[a,h,1], Haohao Cui[a], Huiying Chen[a], Zhikang Wu[d], Hong Chen[c], Hai Li[d], Zhan Zhou[a,b,*], Meiting Zhao[e,*], Chaoliang Tan[f,g,*], Jingguo Li[a,*]

[a] Henan Provincial People's Hospital, People's Hospital of Zhengzhou University, Zhengzhou 450003, China
[b] College of Chemistry and Chemical Engineering, Henan Key Laboratory of Function-Oriented Porous Materials, Luoyang Normal University, Luoyang 471934, China
[c] Luoyang Key Laboratory of Organic Functional Molecules, College of Food and Drug, Luoyang Normal University, Luoyang 471934, China
[d] Institute of Advanced Materials (IAM) and Key Laboratory of Flexible Electronics (KLoFE), Nanjing Tech University (NanjingTech), Nanjing 211816, China
[e] Department of Chemistry, Institute of Molecular Aggregation Science, Tianjin Key Laboratory of Molecular Optoelectronic Sciences, Tianjin University, Tianjin 300072, China
[f] Department of Chemistry and Center of Super-Diamond and Advanced Films (COSDAF), City University of Hong Kong, Hong Kong 999077, China
[g] Shenzhen Research Institute, City University of Hong Kong, Shenzhen 518057, China
[h] Pharmaceutical Sciences Laboratory, Åbo Akademi University, Turku 20520, Finland

ARTICLE INFO

Article history:
Received 13 October 2022
Revised 9 January 2023
Accepted 10 January 2023
Available online 14 January 2023

Keywords:
2D nanosheets
PCN-134 MOFs
Size effect
Photodynamic therapy
Antibacterial

ABSTRACT

Although porphyrin-based metal-organic frameworks (MOFs) have been widely explored as photosensitizers for photodynamic therapy, how the size will affect the light-induced catalytic activity for generation of reactive oxygen species (ROS) still remain unclear. Herein, we first report the size-controlled synthesis of two-dimensional (2D) porphyrin-based PCN-134 MOF nanosheets by a two-step solvothermal method to explore the size effect on its PDT performance, thus yielding enhanced photodynamic antimicrobial therapy. By simply controlling the reaction temperature in the synthesis process, the bulk PCN-134 crystal, large PCN-134 (L-PCN-134) nanosheets with a lateral size of 2–3 μm and thickness of 33.2–37.5 nm and small PCN-134 nanosheets (S-PCN-134) with a lateral size of 160–180 nm and thickness of 9.1–9.7 nm were successfully prepared. Interestingly, the S-PCN-134 nanosheets exhibit much higher photodynamic activity for ROS generation than that of the bulk 3D PCN-134 crystal and L-PCN-134 nanosheets under a 660 nm laser irradiation, suggesting that the photodynamic activity of PCN-134 MOF increases when the size reduces. Therefore, the S-PCN-134 nanosheets show much enhanced performance when used as a photosensitizer for photodynamic antimicrobial activity and wound healing.

Due to the long-term abuse of antibiotics, more and more strains have developed resistance to antibiotics, which is a huge challenge to human life and health [1–4]. Therefore, many antibacterial strategies have been developed, such as the release of metal ions [5–7], photothermal therapy [8–12], chemodynamic therapy [13–16], nanoenzyme-catalyzed therapy [17–19], sonodynamic therapy [11,20,21], and photodynamic therapy (PDT) [22–28]. Among them, PDT has been demonstrated to be a promising method to kill bacteria with less invasive and negligible side effects due to the photosensitizer can transfer the light energy to O_2 to produce reactive oxygen species (ROS). Organic molecules, including indocyanine green, hypocrellin B, porphyrin and its derivatives, are the widely explored photosensitizers due to their abilities to produce $^1O_2$ under light irradiation, which can effectively resist bacteria [29–33]. Among them, porphyrin and its derivatives have been considered the effective photosensitizers for PDT due to their excellent photophysical properties and large π-conjugated aromatic domains to enhance the generation of $^1O_2$ [34,35]. However, the porphyrin-based photosensitizers suffer from the poor water solubility, easy aggregation, and photobleaching, thus significantly limiting their performance in PDT [36,37]. Introducing porphyrin into an ordered material framework can not only effectively avoid intermolecular aggregation, but also enhance the stability of porphyrin, which is expected to improve its photodynamic property.

Metal-organic frameworks (MOFs) are a class of porous materials, which are composed of metal and organic ligands connected

* Corresponding authors.
E-mail addresses: zhouzhan@lynu.edu.cn (Z. Zhou), mtzhao@tju.edu.cn (M. Zhao), chaoltan@cityu.edu.hk (C. Tan), lijingguo@zzu.edu.cn (J. Li).
[1] These authors contributed equally to this work.

https://doi.org/10.1016/j.cclet.2023.108140
1001-8417/

by coordination bonds [38–49]. Porphyrin-based organic molecules have been widely used as ligands for construction of porphyrin-based MOFs for various applications including photodynamic cancer therapy and antibacterial [50–53]. Compared to the organic porphyrin-based photosensitizers, the porphyrin-based MOFs have periodically ordered porphyrins that are separated by the metal-oxygen clusters, thus effectively avoiding the aggregation and self-quenching of photosensitizers. As a typical example, the Cu^{II}-metalated porphyrin-based MOF has been constructed for enhanced photodynamic therapy under the tumor specific microenvironment due to the decrease of glutathione by the reacting with Cu component to realize the improvement of ROS [54]. In addition, Lou *et al*. found that reduction the dimensional of porphyrin-based MOF from three-dimensional (3D) to two-dimensional (2D) can effectively increase its specific surface area, which can promote the energy transfer from photosensitizer to O_2 and the diffusion of $^1O_2$ to significantly enhance the photodynamic tumor therapy [49]. Recently, the porphyrin-based MOFs have also been used in photodynamic antibacterial therapy. For example, PCN-224 (PCN stands for porous coordination network) have been coated on the surface of cotton fabric by *in situ* growth to fabricate the light-driven antibacterial cotton fabric for effective PDT antibacterial, which can effectively generate $^1O_2$ under the light irradiation [55]. Liu *et al*. proved that the topological structure of porphyrin-based MOFs has great influence on their photodynamic properties [56]. They found that MOF-545 with the large pore size, and long distances between inter-porphyrinic active sites exhibited superior PDT performance to those of MOF-525, PCN-224, and PCN-223. However, the influence of the size of porphyrin-based MOFs on the generation of ROS and photodynamic antimicrobial therapy have not been reported.

Herein, we first report the controlled synthesis of porphyrin-based 2D PCN-134 MOF nanosheets by a two-step solvothermal method for enhanced photodynamic antimicrobial therapy (Scheme 1). The size and thickness of 2D PCN-134 nanosheets can be controlled by changing reaction temperatures at the first solvothermal step. Compared to the PCN-134 bulk crystal (B-PCN-134) and 2D large PCN-134 (L-PCN-134) nanosheets, the 2D small PCN-134 (S-PCN-134) nanosheets exhibit higher catalytic activity for ROS generation under a 660 nm laser irradiation, which can be used as an efficient photosensitizer for enhanced photodynamic therapy. After modifying by polyvinylpyrrolidone (PVP), the PVP@S-PCN-134 nanosheets show excellent photodynamic antibacterial performance than that of 3D PCN-134 crystal or 2D large PCN-134 nanosheets. Therefore, the PVP@S-PCN-134 nanosheets can realize photodynamic antibacterial *in vitro* and promote wound healing *in vivo*.

The PCN-134 bulk crystal was prepared by a two-step solvothermal method according to the previously report [57]. $ZrCl_4$ and the organic linker 1,3,5-tri(4-carboxyphenyl) benzene (BTB) were assembled into 2D layer (Zr-BTB) using low temperature at the first solvothermal step, and then the other linker *meso*-tetra(4-carboxyphenyl)porphyrin (TCPP) was added to assemble the 3D PCN-134 crystal by the high temperature at the second step. The scanning electron microscopy (SEM) image of bulk PCN-134 crystal displays large size (~15 μm) with a regular hexagonal shape (Fig. S1a in Supporting information), and its powder X-ray diffraction (XRD) peaks are consistent with the simulated data (Fig. S1b in Supporting information), indicating the successful preparation of the bulk PCN-134 crystal (denoted as B-PCN-134). The preparation of PCN-134 nanosheets are achieved by changing types of zirconium salt, organic acid, and the temperature at the first solvothermal step (see the Experimental Section in Supporting information). It was found that the size of nanosheets gradually decreased with the increasing temperature at the first step. When the reaction temperature kept at 100 °C in the first step, the PCN-134 nanosheets with large lateral size and thicker thickness were obtained. The SEM images clearly show that the large PCN-134 (denoted as L-PCN-134) nanosheets have a regular hexagonal shape with an average size of 2–3 μm (Fig. 1a), which was further verified in their transmission electron microscopy (TEM) image (Fig. 1b). As shown in Fig. 1c, the high-resolution TEM image of a typical L-PCN-134 nanosheet displays the distinct lattice fringes, and the lattice distance was measured as 1.68 nm, which is corresponding to the (010) plane of the PCN-134 crystal [58]. The thickness of this L-PCN-134 nanosheets is about 33.2–37.5 nm, which is measured from its atomic force microscopy (AFM) height images (Fig. 1d, and Fig. S2 in Supporting information). Interestingly, when the temperature of the first step kept at 120 °C, the PCN-134 nanosheets with small lateral size and thinner thickness were obtained. The small PCN-134 (S-PCN-134) nanosheets have a size

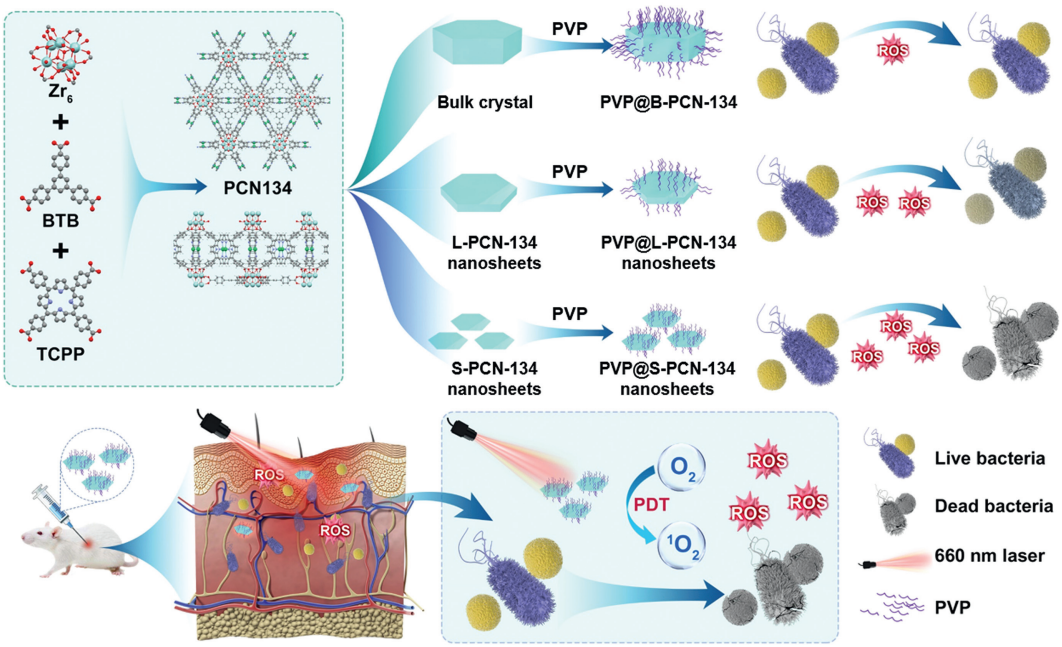

Scheme 1. Schematic diagram of controlled synthesis of 2D PCN-134 MOF nanosheets and their applications for enhanced photodynamic antimicrobial therapy.

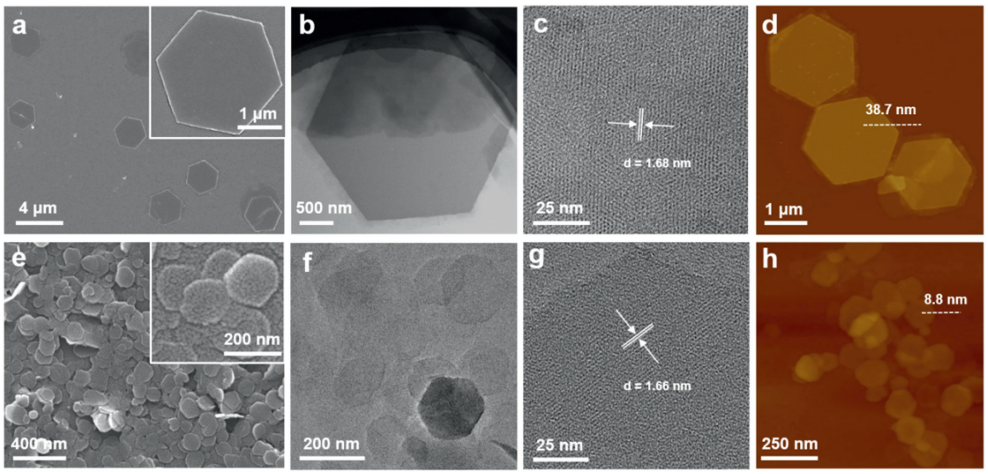

Fig. 1. The SEM image of (a) large and (e) small PCN-134 nanosheets. The (b, f) low-resolution and (c, g) high-resolution TEM images of large and small PCN-134 nanosheets. The AFM images of (d) large and (h) small PCN-134 nanosheets.

about 160–180 nm (Fig. 1e), which was also verified by the TEM image (Fig. 1f). Interestingly, the obtained S-PCN-134 nanosheets still give the clear lattice stripes in the high-resolution TEM image (Fig. 1g), and the lattice distance was measured as 1.66 nm, which is consistent with that of L-PCN-134 nanosheets. The AFM height images of S-PCN-134 nanosheets show that its thickness is 9.1–9.7 nm, proving its ultrathin characteristic (Fig. 1h, and Fig. S3 in Supporting information). The crystal structures of L-PCN-134 and S-PCN-134 nanosheets were proved by the XRD. As shown in Fig. S4 (Supporting information), all the characteristic peaks of the large and small PCN-134 nanosheets were consistent with those of its single crystal simulation, proving they had the same crystal structure even though their microscopic morphology was different.

The L-PCN-134 and S-PCN-134 nanosheets were also studied by X-ray photoelectron spectroscopy (XPS). It can be seen from the XPS full spectra (Fig. S5a in Supporting information) that both the L-PCN-134 and S-PCN-134 nanosheets contained Zr, C, N, and O elements, which was further proving they had the same elemental composition. As shown in high-resolution Zr 3d XPS spectra of both the L-PCN-134 and S-PCN-134 nanosheets (Fig. S5b in Supporting information), there were two main characteristic peaks at 182.58 eV and 184.83 eV, corresponding to the $3d_{5/2}$ of Zr and the $3d_{3/2}$ of Zr spin-orbit peaks, respectively. The C 1s spectrum (Fig. S5c in Supporting information) exhibited the C–C and C=O peak at 284.88 and 288.88 eV, respectively. It shows the characteristic peak of N 1s (Fig. S5d in Supporting information) at 399.78 eV and the characteristic peak of O 1s (Fig. S5e in Supporting information) at 531.98 eV, which all verify the successful preparation of the L-PCN-134 and S-PCN-134 nanosheets.

Porphyrin and its derivatives have good photodynamic activity due to their abilities to produce $^1O_2$ under the light irradiation. To investigate the photodynamic performance of B-PCN-134, L-PCN-134 and S-PCN-134 nanosheets, the commercial singlet oxygen sensor green (SOSG) was chosen to monitor the production of $^1O_2$. There was almost no fluorescence in the free SOSG solution, while it would exhibit strong green emission with the maximum wavelength of 525 nm in the presence of $^1O_2$. The final concentration of the B-PCN-134 was kept at 50 μg/mL. After irradiation using a near infrared (NIR) light (660 nm, 0.5 W/cm^2) for 5 min, the fluorescence intensity of the SOSG solution slightly increased (Fig. 2a), suggesting that B-PCN-134 could generate $^1O_2$ under the irradiation. As shown in Fig. 2b, when adding L-PCN-134 nanosheets into the SOSG solution, its fluorescence intensity at 525 nm was 2.5 times higher, compared to that of the B-PCN-134. Promisingly, the fluorescence intensity of SOSG solution in the presence of S-PCN-134

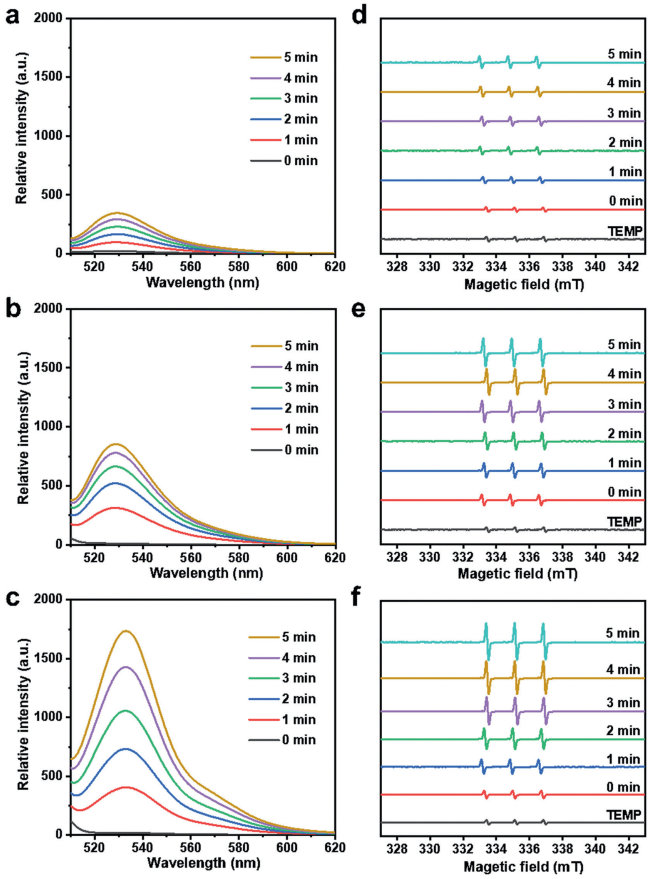

Fig. 2. Fluorescence spectra of SOSG solution with the addition of 50 μg/mL of (a) B-PCN-134 crystal, (b) L-PCN-134, and (c) S-PCN-134 nanosheets under a 660 nm laser (0.5 W/cm^2) irradiation for 5 min. ESR spectra of (d) B-PCN-134 crystal, (e) L-PCN-134, and (f) S-PCN-134 nanosheets under a 660 nm laser (0.5 W/cm^2) irradiation for different time.

nanosheets was even higher (Fig. 2c), which was 6.5 times in the comparison with that of B-PCN-134. These results indicated that S-PCN-134 nanosheets had the strongest ability to produce $^1O_2$. Additionally, the influence of the power of the lamp on the ability of S-PCN-134 nanosheets to produce $^1O_2$ was also detected. As shown in Fig. S6 (Supporting information), the generation $^1O_2$ of the S-PCN-134 nanosheets was gradually enhanced with the increas-

ing powder of lamp. Furthermore, electron spin resonance (ESR) spectrum was also used to detect $^1O_2$ from B-PCN-134, L-PCN-134 and S-PCN-134 using 2,2,6,6-tetramethylpiperidine (TEMP) as the spin trapping agent. It can be seen that the amplitude of ESR peaks in the B-PCN-134 is very limited under the illumination for 5 min in the comparison to that of free TEMP (Fig. 2d), indicating that the $^1O_2$ production of B-PCN-134 is very low. As for the PCN-134 nanosheets, the ESR signal of both L-PCN-134 (Fig. 2e) and S-PCN-134 (Fig. 2f) are obviously stronger than those of bulk under the same irradiation condition. Promisingly, the ESR signal of the S-PCN-134 nanosheets is the strongest among the three MOFs with different size, further revealing that the S-PCN-134 nanosheets exhibit the strongest ability to generate $^1O_2$ under light irradiation.

To improve the biological stability of PCN-134 under physiological environment, polyvinylpyrrolidone (PVP) was used to modify the surfaces of B-PCN-134, L-PCN-134, and S-PCN-134 nanosheets to obtain the PVP@B-PCN-134, PVP@L-PCN-134, PVP@S-PCN-134 nanosheets, respectively. Subsequently, the photodynamic antibacterial properties of them were evaluated in both *Staphylococcus aureus* (*S. aureus*) and *Escherichia coli* (*E. coli*) by the colony method. As for *S. aureus* (Fig. 3a), the number of colonies were almost no changes for all the groups including PBS control, PVP@B-PCN-134, PVP@L-PCN-134, PVP@S-PCN-134 nanosheets (50 μg/mL), suggesting they had low dark toxicity. After irradiating by a 660 nm laser (0.5 W/cm^2) for 5 min, the bacterial survival rate of PVP@B-PCN-134 and PVP@L-PCN-134 nanosheets maintained 100% and 85.1%, respectively (Fig. 3b), while only 3.7% of the bacteria survived in the PVP@S-PCN-134 nanosheets group. Interestingly, *S. aureus* almost disappeared when the irradiation time was extended to 10 min in the PVP@S-PCN-134 nanosheets group (Figs. 3a and b). When the concentration of PVP modified PCN-134 increased to 100 μg/mL, the bacteriostatic rate of small nanosheets reached 97.5% under the irradiation for 5 min, while those of bulk and large nanosheets only reached 0.8% and 66.5% even if the irradiation time was extended to 10 min (Fig. 3c), indicating that the smaller size and thinner thickness promoted the PDT effect of PCN-134 and enhanced its antibacterial effect. We further tested the antibacterial effect of PVP@S-PCN-134 nanosheets for *E. coli* under the irradiation by the same laser (660 nm, 0.5 W/cm^2). As shown in Fig. S7 (Supporting information), it can be seen that the bacteriostatic concentration and time of PVP@S-PCN-134 nanosheets against *E. coli* were 100 μg/mL and 30 min, respectively, both of which were higher than those against *S. aureus* (50 μg/mL for 10 min, or 100 μg/mL for 5 min).

To verify the antimicrobial efficacy of the PVP@S-PCN-134 nanosheets in wound healing, the mice infected wound model was artificially conducted. All protocols for animal assays were approved by the Institutional Animal Care and Use Committee (IACUC) of Henan Provincial People's Hospital. As a control, a group of mice was applied with PBS (I), and another group (II) was applied with PBS + NIR laser (660 nm, 0.5 W/cm^2, 10 min). PVP@S-PCN-134 nanosheets without (III) and with (IV) NIR laser (660 nm, 0.5 W/cm^2, 10 min) were subsequently applied onto the wound areas, respectively. The details of the treatment were summarized in Fig. S8 (Supporting information). The healing processes of these groups were recorded on day 0, 1, 3, 5, 7 and 9. After 9 days of healing, purulent water leakage was still observed in control group and PBS + NIR group, the wound healing effect of the PVP@S-PCN-134 nanosheets + NIR group was obviously superior to other groups (Fig. 4a). On the day 5, the wound area of the PVP@S-PCN-134 nanosheets + NIR group reduced to 52.5% ± 3.97%, and 14.5% ± 2.87% on day 9 which was also the smallest on day 9 among all groups (Fig. S9 in Supporting information). According to the observation on day 9, the PBS group remained as high as 32.7% ± 6.77%, 40.3% ± 10.27% and 26.3% ± 8.82% were achieved in the PBS + NIR group and PVP@S-PCN-134 nanosheets group, respectively (Fig. S9). On the 3rd day of healing, wound tissues of all groups were collected and applied in TSB plate after homogenization for colony counting. The bacterial survival rate of the PBS + NIR group was

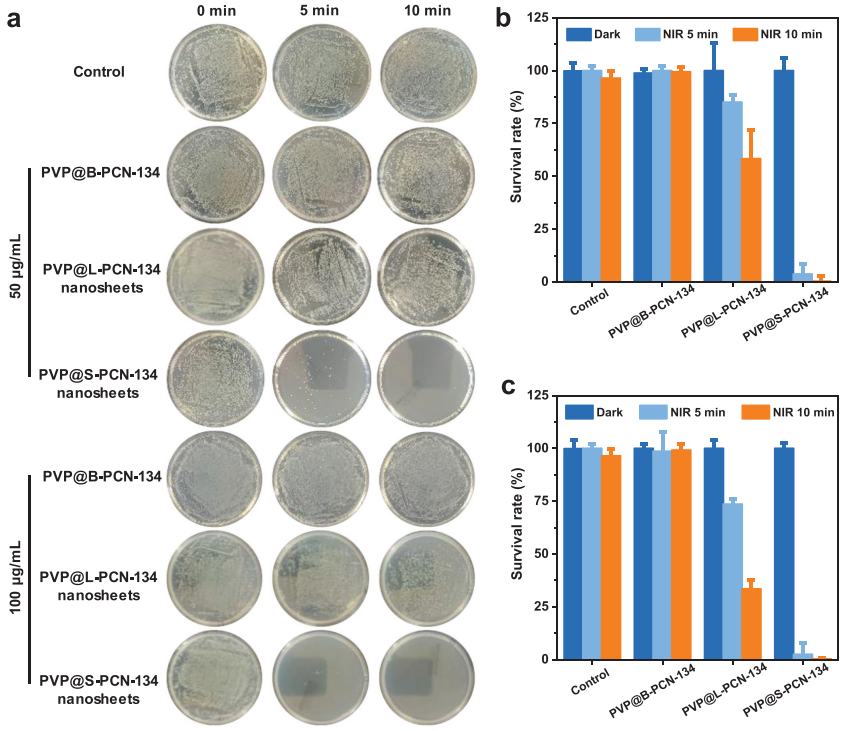

Fig. 3. Antibacterial effects of PVP@PCN-134 under 660 nm (0.5 W/cm^2) laser irradiation. (a) Photographs of *S. aureus* on agar plates treated with different conditions. (b) Survival rate of *S. aureus* was calculated with plate count method when the concentration of PCN-134 was 50 μg/mL. (c) Survival rate of *S. aureus* was calculated with plate count method when the concentration of PCN-134 was 100 μg/mL.

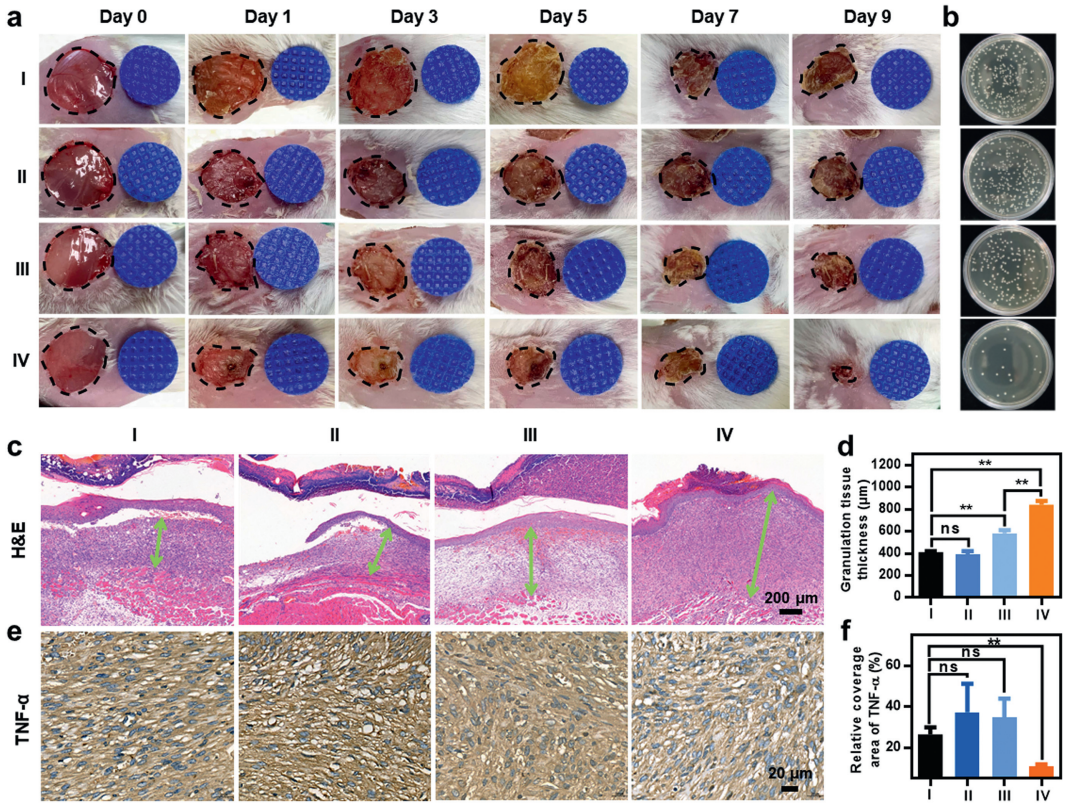

Fig. 4. (a) Representative pictures of wound infection in mice treated with PBS (I), PBS + NIR (II), S-PCN-134 nanosheets (III), S-PCN-134 nanosheets + NIR (IV) for different days. (b) Colony photographs of mice wound tissue in different treatment groups after 3 days. (c) H&E staining images of the wound tissue sections after different treatments after 9 days. (d) Granulation tissue thickness in different treatments. $n = 5$. $^{**}P < 0.01$, ns: no statistical significance. (e) TNF-α images of the wound tissue sections after different treatments after 9 days. (f) Relative coverage area of TNF-α of the wound tissue sections after different treatments. $n = 5$. $^{**}P < 0.01$, ns: no statistical significance.

almost the same as that of the PBS group, while the PVP@S-PCN-134 nanosheets + NIR group had the lowest bacterial survival rate (Fig. 4b and Fig. S10 in Supporting information), followed by the PVP@S-PCN-134 nanosheets group, indicating the PVP@S-PCN-134 nanosheets irradiated by NIR laser (660 nm) had significant antibacterial application in wound healing.

The granulation tissue regenerated at the wound area after healing was also analyzed by H&E staining. Benefited from the excellent antibacterial capability of the PVP@S-PCN-134 nanosheets, the regenerated granulation tissue of PVP@S-PCN-134 nanosheets + NIR group grew the fastest and reached 0.84 ± 0.03 mm in thickness (Figs. 4c and d), while the granulation tissue thickness of control group was only 0.41 ± 0.01 mm, that of PBS + NIR group was 0.39 ± 0.029 mm. Additionally, the thickness of the granulation tissue of the wound treated with PVP@S-PCN-134 nanosheets without NIR laser was 0.58 ± 0.03 mm, which was smaller than the PVP@S-PCN-134 nanosheets + NIR group, and larger than the other groups (Figs. 4c and d). These results suggested that the PVP@S-PCN-134 nanosheets + NIR presented an effect of promoting wound healing and granulation tissue regeneration. Importantly, the weight of mice in all groups was measured every day, and there were no significant weight changes in both PVP@S-PCN-134 nanosheets and PVP@S-PCN-134 nanosheets + NIR groups compared to that of PBS group (Fig. S11 in Supporting information), indicating PVP@S-PCN-134 nanosheets exhibited the excellent biocompatibility.

To demonstrate the anti-infection performance of the PVP@S-PCN-134 nanosheets, immunohistochemical analysis was used to investigate the expression of tumor necrosis factor-α (TNF-α) in the wound area. TNF-α is a typical proinflammatory factor, and its expression level can reflect the inflammation level induced by bacteria infection in wound healing process. As shown in Fig. 4e, TNF-α expression was significantly lower in the PVP@S-PCN-134 nanosheets + NIR group, the coverage area was 10.96% ± 0.94% compared with 37.32% ± 13.90% of the PBS + NIR group and 34.95% ± 9.04% of the PVP@S-PCN-134 nanosheets group (Fig. 4f). This might be attributed to its antibacterial effect and the wounds could be effectively protected against bacterial infection to avoid severe inflammatory response.

In summary, we have achieved the size-controlled synthesis of 2D PCN-134 MOF nanosheets by a two-step solvothermal method and exploration of size effect on its photodynamic performance, thus realizing enhanced performance for photodynamic antibacterial therapy. The 2D PCN-134 nanosheets with different lateral size and thickness were successfully prepared by controlling the reaction temperature. Importantly, the photodynamic activity of the PCN-134 MOF for ROS generation under 660 nm laser irradiation increases when the size reduces and both the L-PCN-134 and S-PCN-134 nanosheets exhibited higher photodynamic activity than that of the B-PCN-134. Therefore, after PVP modification, the PVP@S-PCN-134 nanosheets can serve as a highly efficient photosensitizer for photodynamic antibacterial therapy. Both *in vitro* and *in vivo* results revealed that the PVP@S-PCN-134 nanosheets can effectively eliminate bacteria and heal wound under the 660 nm laser irradiation. Our study confirms that the size has a significant effect on the photodynamic performance of PCN-134 MOFs. It is believed that such a size engineering can be further extended to other MOF materials and other materials.

Declaration of competing interest

The authors declare that they have no known competing financial interests or personal relationships that could have appeared to influence the work reported in this paper.

Acknowledgments

Z. Zhou thanks the funding support from the National Natural Science Foundation of China (No. 52102348), the Science and Technology Innovation Talent Program of University in Henan Province (No. 23HASTIT016), and the funding support from China Postdoctoral Science Foundation (No. 2021M701113). J. Li thanks the funding support from the National Natural Science Foundation of China (No. 52173143). C. Tan thanks the funding support from the National Natural Science Foundation of China (No. 22005259) and the Start-Up Grant (No. 9610495) from City University of Hong Kong. M. Zhao thanks the funding support from the National Natural Science Foundation of China (No. 21905195), Natural Science Foundation of Tianjin City (No. 20JCYBJC00800), and the PEIYANG Young Scholars Program of Tianjin University (No. 2020XRX-0023).

Supplementary materials

Supplementary material associated with this article can be found, in the online version, at doi:10.1016/j.cclet.2023.108140.

References

[1] M.C. Fisher, A. Alastruey-Izquierdo, J. Berman, et al., Nat. Rev. Microbiol. 20 (2022) 557–571.
[2] S. Tong, H. Bambrick, P.J. Beggs, et al., Environ. Int. 158 (2022) 106892.
[3] Z. Guo, L. Shi, H. Feng, et al., Chin. Chem. Lett. 32 (2021) 1046–1050.
[4] T. Hu, Z. Gu, G.R. Williams, et al., Chem. Soc. Rev. 51 (2022) 6126–6176.
[5] F. Hu, B. Song, X. Wang, et al., Chin. Chem. Lett. 33 (2022) 308–313.
[6] T. Yang, D. Wang, X. Liu, J. Mater. Chem. B 8 (2020) 406–415.
[7] Y. Yang, X. Wu, C. He, et al., ACS Appl. Mater. Interfaces 12 (2020) 13698–13708.
[8] Z. Zhou, X. Li, T. Hu, et al., Adv. NanoBiomed Res. 2 (2022) 2200065.
[9] H. Huang, J. Zha, S. Li, et al., Chin. Chem. Lett. 33 (2022) 163–176.
[10] L. Dang, T. Li, T. Zhang, et al., Chem. Sci. 13 (2022) 5130–5140.
[11] X. He, J. Hou, X. Sun, et al., Adv. Funct. Mater. 32 (2022) 2203964.
[12] Z. Zhou, B. Li, C. Shen, et al., Small 16 (2020) 2004173.
[13] X. Zhao, X. He, A. Hou, et al., Inorg. Chem. 61 (2022) 9328–9338.
[14] X. He, L. Dai, L. Ye, et al., Adv. Sci. 9 (2022) 2105223.
[15] Y. Li, X. Liu, Z. Cui, et al., ACS Nano 16 (2022) 14860–14873.
[16] Z. Zhou, X. Wang, H. Zhang, et al., Small 17 (2021) 2007486.
[17] X. Wang, Q. Shi, Z. Zha, et al., Bioact. Mater. 6 (2021) 4389–4401.
[18] J. Xi, G. Wei, L. An, et al., Nano Lett. 19 (2019) 7645–7654.
[19] Z. Zhou, Y. Wang, F. Peng, et al., Angew. Chem. Int. Ed. 61 (2022) e202115939.
[20] H. Chen, X. He, Z. Zhou, et al., J. Nanobiotech. 20 (2022) 136.
[21] M. Wu, Z. Zhang, Z. Liu, et al., Nano Today 37 (2021) 101104.
[22] W. Shen, T. Hu, X. Liu, et al., Nat. Commun. 13 (2022) 3384.
[23] J. Sun, Y. Fan, W. Ye, et al., Chem. Eng. J. 417 (2021) 128049.
[24] N. Niu, H. Zhou, N. Liu, et al., Chem. Commun. 55 (2019) 4395–4398.
[25] F. E Q. Jiang, J. Tian, et al., ACS Appl. Mater. Interfaces 12 (2020) 16150–16158.
[26] Q. Xiao, B. Mai, Y. Nie, et al., ACS Appl. Mater. Interfaces 13 (2021) 11588–11596.
[27] G. Boccalini, L. Conti, C. Montis, et al., J. Mater. Chem. B 5 (2017) 2788–2797.
[28] J. Sun, Y. Fan, P. Zhang, et al., J. Colloid Interf. Sci. 559 (2020) 197–205.
[29] X. Ragàs, D. Sánchez-García, R. Ruiz-González, et al., J. Med. Chem. 53 (2010) 7796–7803.
[30] K. Bilici, N. Atac, A. Muti, et al., Biomater. Sci. 8 (2020) 4616–4625.
[31] L. Chen, H. Bai, J. Xu, et al., ACS Appl. Mater. Interfaces 9 (2017) 13950–13957.
[32] X. Wan, Y. Xu, Y. Li, et al., Food Res. Int. 156 (2022) 111141.
[33] Z. Li, J. Zhang, X. Tian, et al., Chem. Sci. 13 (2022) 9381–9386.
[34] D. Wang, L. Niu, Z. Qiao, et al., ACS Nano 12 (2018) 3796–3803.
[35] L. Sobotta, P. Skupin-Mrugalska, J. Piskorz, et al., Eur. J. Med. Chem. 175 (2019) 72–106.
[36] H. Wang, Y. Yang, B. Yuan, et al., ACS Appl. Mater. Interfaces 13 (2021) 2269–2276.
[37] G. Murali, B. Kwon, H. Kang, et al., ACS Appl. Nano Mater. 5 (2022) 4376–4385.
[38] J. Guo, Y. Qin, Y. Zhu, et al., Chem. Soc. Rev. 50 (2021) 5366–5396.
[39] Y. Qin, Y. Wan, J. Guo, et al., Chin. Chem. Lett. 33 (2022) 693–702.
[40] Z. Li, J. Guo, Y. Wan, et al., Nano Res. 15 (2022) 3514–3532.
[41] P. Gao, Y. Jiang, H. Liu, et al., ACS Appl. Mater. Interfaces 14 (2022) 16435–16444.
[42] X. Yang, Z. Zhai, X. Lu, et al., ACS Cent. Sci. 6 (2020) 1169–1178.
[43] Y. Qin, J. Guo, M. Zhao, Trans. Tianjin Univ. 27 (2021) 434–449.
[44] Q. Ding, Z. Xu, L. Zhou, et al., J. Colloid Interf. Sci. 621 (2022) 180–194.
[45] R. Zheng, J. Guo, X. Cai, et al., Colloid. Surface. B 213 (2022) 112432.
[46] C. Chang, W. Chen, Y. Chen, et al., Acta Phys. Chim. Sin. 37 (2021) 2108017.
[47] W. Teo, J. Liu, W. Zhou, et al., SmartMat 2 (2021) 567–578.
[48] Y. Sun, M. Gao, H. Li, et al., Acta Phys. Chim. Sin. 37 (2021) 2007048.
[49] T. Luo, Y. Fan, J. Mao, et al., J. Am. Chem. Soc. 144 (2022) 5241–5246.
[50] W. Zhou, S. Begum, Z. Wang, et al., ACS Appl. Mater. Interfaces 10 (2018) 1528–1533.
[51] X. Li, X. Zhao, D. Chu, et al., Surf. Interfaces 33 (2022) 102247.
[52] J. Liu, Y. Yang, W. Zhu, et al., Biomaterials 97 (2016) 1–9.
[53] Y. Luo, J. Li, X. Liu, et al., ACS Cent. Sci. 5 (2019) 1591–1601.
[54] W. Zhang, J. Lu, X. Gao, et al., Angew. Chem. Int. Ed. 57 (2018) 4891–4896.
[55] X. Nie, S. Wu, A. Mensah, et al., J. Colloid Interf. Sci. 579 (2020) 233–242.
[56] Y. Liu, L. Chen, X. Zhao, et al., Chem. Eur. J. 27 (2021) 10151–10159.
[57] S. Yuan, J. Qin, L. Zou, et al., J. Am. Chem. Soc. 138 (2016) 6636–6642.
[58] M. Zhao, J. Chen, B. Chen, et al., J. Am. Chem. Soc. 142 (2020) 8953–8961.